Pulsatile microfluidics as an analytical tool for determining the dynamic characteristics of microfluidic systems

Søren Vedel[1], Laurits Højgaard Olesen[2] and Henrik Bruus[1]

[1] Department of Micro- and Nanotechnology, Technical University of Denmark, DTU Nanotech
Building 345 East, DK-2800 Kongens Lyngby, Denmark
[2] Device Research and Technology, Novo Nordisk A/S, Brennum Park, DK-3400 Hillerød, Denmark

E-mail: Henrik.Bruus@nanotech.dtu.dk

Abstract

An understanding of all fluid dynamic time scales is needed to fully understand and hence exploit the capabilities of fluid flow in microfluidic systems. We propose the use of harmonically oscillating microfluidics as an analytical tool for the deduction of these time scales. Furthermore, we suggest the use of system-level equivalent circuit theory as an adequate theory of the behavior of the system. A novel pressure source capable of operation in the desired frequency range is presented for this generic analysis. As a proof of concept, we study the fairly complex system of water-filled interconnected elastic microfluidic tubes containing a large, trapped air bubble and driven by a pulsatile pressure difference. We demonstrate good agreement between the system-level model and the experimental results, allowing us to determine the dynamic time scales of the system. However, the generic analysis can be applied to all microfluidic systems, both ac and dc.

(Some figures in this article are in colour only in the electronic version)

1. Introduction

The fluid flow of almost all microfluidic systems so far presented in the literature operates in a steady state. Though some of the recently presented highly parallelized systems depend on on-chip dynamics, such as the system of Thorsen *et al* [1] consisting of 256 sub-nanoliter reaction chambers and 2056 microvalves, the flow of liquid is almost exclusively in a steady state. This is because the system is run for enough time that any temporal effects such as fluid inertia and system compliance have died out. In fact, this independence of time is to many one of the attractions of microfluidics. Apart from the inherently time-dependent valves, which have been studied for some time—see e.g. the work of Olsson *et al* [2] or Brask *et al* [3]—few microfluidic systems have been designed to exploit these temporal dependencies. A recent example is the passive on-chip switch of Leslie *et al* [4], which requires an externally applied harmonically oscillating pressure gradient to drive the fluid. Elastic membranes on the chip act as sources of compliance, which are expanded when the fluid pressure inside

the chip increases, and the expanded volume is filled with incoming fluid. This fluid can be thought of as stored in the compliant membrane. The converse happens when the fluid pressure in the system decreases: the membrane contracts and a volume of fluid is pushed out (negative storage). When the oscillation frequency is so fast that this expanding/contracting motion does not have time to occur, the fluid flow will never reach a steady state and very little of it will have time to flow downstream; the volume of fluid that has been moved downstream of the compliant medium is less than would have been the case, had the fluid moved in a steady state. Using two channels of different liquid inertias and tuning the driving frequency, the chip of Leslie *et al* displays a switching behavior where the flow in one channel is amplified while the flow in the other is impeded.

Whether one is designing an 'ac' or 'dc' system, full exploitation of the system requires the understanding of all transient effects. For the system of Thorsen *et al* the chemical reactions could be compromised if insufficient volumes of fluid are delivered to the chambers as a consequence of long

transient time scales. On the other hand, waiting much longer than needed for the fluid to reach a steady state limits the system throughput. The ac system of Leslie *et al* hinges critically on the correct tuning of the compliance time scales of the two channels of the switch. Clearly, understanding and exploitation of the transient fluidic effects are required to fully realize the potential of lab-on-a-chip systems as a significant improvement to 'regular' laboratories.

A common method for studying the dynamics of a physical system is to use harmonically oscillating external fields, which allow for the study of all time scales of the system by sweeping the oscillation frequency. For a typical microfluidic system, pulsatile (harmonically oscillating) driving pressure would be the typical choice of the external field. By studying the frequency response of the microfluidic system, the various time scales are found, and the dominating time scale can be determined. As illustrated above, these time scales set the upper limit for when the system reaches a steady state, and are thus important parameters when more than one operation is to occur on the chip.

An estimate of the typical transient time scales of a microfluidic system can be given by considering the start-up of a pressure driven flow. Such a flow will accelerate and approach the steady state solution of the Hagen–Poiseuille law asymptotically with a characteristic time τ [5]. For a circular cross section, τ is given by

$$\tau = \frac{a^2}{\gamma_1^2 \nu}, \tag{1}$$

where a is the tube radius, ν is the kinematic viscosity of the liquid and $\gamma_1 = 2.4048$ is the first root of the Bessel function of the first kind of order 0 (see table 1 for a list of parameters). For a water-filled tube of $a \sim 100$ μm this time scale is $\tau \sim 1.7$ ms, so in order to use pulsatile microfluidics, a driving mechanism capable of probing frequencies into the low kilohertz range is needed. Secondly, this driving mechanism should deliver characteristic volumes of $\mathcal{V} \sim 0.1$ mm^3 per cycle. This is to ensure that a volume sufficiently larger than the characteristic volume of a generic microfluidic system (e.g. [1, 6]) is delivered by each stroke, thus rendering the flow in the system fully pulsatile.

Lumped parameter modeling in microfluidics consists of modeling the system of consideration as a network of ideal hydraulic resistances R_{hyd}, inertances L_{hyd} and compliances C_{hyd}, corresponding respectively to viscous losses, inertial losses and volume storage (departure from rigid confinement) [2, 4, 7–10]. The components depend on various system parameters such as tube radius, fluid viscosity, etc. The method is known as equivalent circuit (EC) theory due to the mathematical equivalency to electric circuits which extends so far that Kirchoffian network analysis may be applied to the microfluidic network, and it is therefore customary to represent the microfluidic circuit by its equivalent electric circuit, see e.g. figure 9. By direct analogy to electric circuits there are three dynamic time scales in microfluidics: $\tau_{RC} = R_{\text{hyd}} C_{\text{hyd}}$, $\tau_{LR} = L_{\text{hyd}}/R_{\text{hyd}}$ and $\tau_{LC} = \sqrt{L_{\text{hyd}} C_{\text{hyd}}}$. Although derived for components, the linearity of the governing Stokes equation of fluid flow assures the validity of the modeling approach to

Table 1. List of parameters, alphabetized by symbol.

Parameter	Symbol	Unit/value
Area	$\mathcal{A}$	m^2
Inner radius	a	m
Compliance	C_{hyd}	m^3 Pa^{-1}
Young's modulus	E	Pa
Frequency	f	Hz
Wall thickness	h	m
Electric current	I	A
Bessel function the first kind of order n	J_n	–
Membrane spring constant	k	N m^{-1}
Actuator force constant	k_{F}	N A^{-1}
Electric inductance	L_{el}	V s A^{-1}
Hydraulic inertance	L_{hyd}	Pa s^2 m^{-3}
Tube length	ℓ	m
Plunger mass	M	kg
Power	P	J s^{-1}
Pressure	p	Pa
Flow rate	Q	m^3 s^{-1}
Pressure source chamber flow rate	Q_{c}	m^3 s^{-1}
Electric resistance	R_{el}	V A^{-1}
Hydraulic resistance	R_{hyd}	Pa s m^{-3}
Radial coordinate	r	m
Period	T	s
Time	t	s
Voltage	U	V
Wall radial displacement	u_r	m
Volume	$\mathcal{V}$	m^3
Chamber volume	$\mathcal{V}_{\text{c}}$	m^3
Initial chamber volume	$\mathcal{V}_{\text{init}}$	m^3
Tent volume	$\mathcal{V}_{\text{tent}}$	m^3
Velocity	v	m s^{-1}
Axial fluid velocity	v_x	m s^{-1}
Coil velocity	v_{coil}	m s^{-1}
Plunger coordinate	x	m
Bubble relative coordinate	x_{rel}	m
Hydraulic impedance	Z_{hyd}	Pa s m^{-3}
Womersley number	α	–
Critical Womersley number	α_{c}	α/γ_1
First root of J_0	γ_1	2.4048
Wall compliance constant	β	–
Dynamic viscosity	η	Pa s
Momentum diffusion length	λ_{d}	m
Kinematic viscosity	ν	m^2 s^{-1}
Density	ρ	kg m^{-3}
Poisson's ratio	σ	–
Dynamic time scale	τ	s
Angular frequency	ω	rad s^{-1}

full system-level analysis [11, 12]. The work of these authors demonstrates the very good level of accuracy attainable by these models for both steady-state and dynamic systems.

In this paper we suggest the use of experimental pulsatile microfluidics in connection with EC theory as an analytical tool for the derivation of the time scales for any microfluidic system. The use of the predictive capabilities of time-dependent EC theory have already been demonstrated for a component by Kim *et al* [9], who derived the compliance of a silicone rubber tube from the characteristic time of the build-up of pressure, and by Leslie *et al* [4], who as previously mentioned generated an on-chip switch by use of rectifying valves and an externally driven ac flow. However,

the use of pulsatile microfluidics allows for the deduction of the time scale of any time-dependent component within any microfluidic system, as long as a valid model of the system is in place. The analysis will allow for the experimental determination of these time scales, while system-level EC analysis will provide a theory to which the experimental results can be compared. The analysis applies to both ac and dc microfluidic systems, since even systems intended for dc operation have inherent dynamic time scales, as mentioned previously. Since the EC elements are given in terms of system parameters, deviations between model results and experimental data will strongly indicate which parameter of the model is incorrect. However, the real strength of the approach lies in the fact that one often has components of unknown compliance in the microfluidic system, such as oddly shaped membranes, valves, trapped gas bubbles etc, which then may be determined using the suggested approach. For example, for many of the bubble-based microfluidic applications such as pumps [13, 14], valves [15, 16], sensors [17, 18] and actuators [19, 20] the approach can be used to verify the bubble size and hence the performance of the system.

As a proof of concept we will in the following expose a full-microfluidic network containing one component of unknown compliance to a pulsatile pressure difference. In addition to the unknown compliance, this ac network consists of interconnected elastic tubing with one large moving air bubble and several stationary compliances of known value. We use system-level EC analysis to model the system in order to derive a numerical value for said compliance while also proving the sufficiency of system-level EC modeling. We note, however, that this generic method of using pulsatile microfluidics is by no means limited to only this purpose. A novel pulsatile pressure source capable of probing the desired low-kilohertz frequencies will be presented and the appropriate EC circuit elements for the proof-of-concept experiment will be derived.

2. The physics of pulsatile flow

The analytical solution to pulsatile flow void of start-up effects is usually credited to Womersley [21], although the problem has been solved independently by several scholars [22–25]. The solution is found by solving the Navier–Stokes equation in cylindrical coordinates and not surprisingly, this solution finds that a harmonically oscillating flow rate arises due to the pulsatile pressure. From a physical standpoint, the fluid flow experiences both viscous resistance and inertia, the latter due to the pulsatility. This is in contrast to the steady-state Poiseuille solution, where only viscous resistance is present.

Womersley's solution depends on the dimensionless Womersley number $\alpha \equiv \sqrt{a^2\omega/\nu}$, where ω is the angular frequency of the pressure oscillations, i.e. $p(t) = \mathrm{Re}[\Delta\tilde{p}\,\mathrm{e}^{\mathrm{i}\omega t}] + p_0$ where the tilde indicates the (in general complex) amplitude and p_0 is a reference pressure. The Womersley number may be interpreted as a non-dimensional measure of the diffusion of momentum: The kinematic viscosity ν is the diffusivity of momentum in the pressure-driven flow [8], while $a^2\omega$ is the diffusivity required for
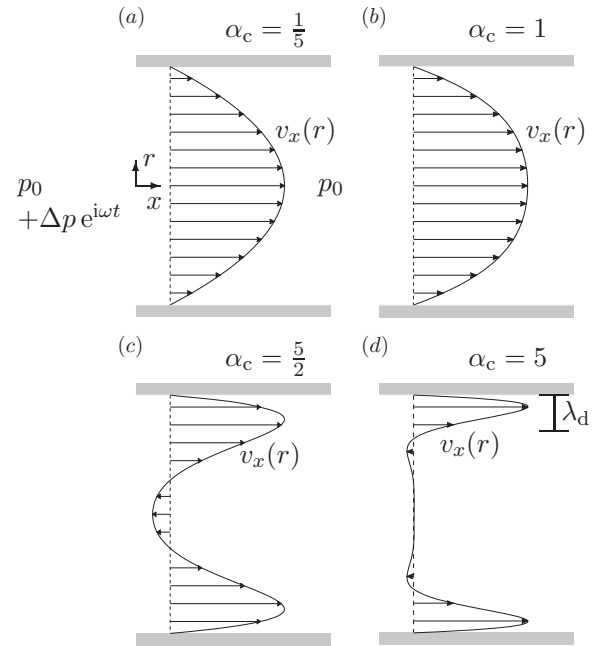

Figure 1. Axial velocity profiles $v_x(r)$ for a liquid with no-slip boundary conditions driven by a pressure difference $\Delta p\,\mathrm{e}^{\mathrm{i}\omega t}$ in a tube, calculated using MATLAB. All velocity profiles are computed at the time $t = T$ for four values of α_c, where T is the oscillation period, and α_c is defined in equation (2). The four velocity profiles are not shown to scale. The direction of the pressure difference is indicated in the figure for $\alpha_c = 1/5$ and is the same for all figures. The effects of inertia on the velocity profile are clearly observable for $\alpha_c > 1$ by the deviation from the Poiseuille paraboloid. The momentum diffusion length $\lambda_d = \sqrt{\nu/\omega}$ giving the width of the quasi-steady annular region is indicated for $\alpha_c = 5$.

momentum to diffuse across the channel before the pressure changes. However, a more intuitive measure may be introduced by considering the inertial relaxation time of equation (1), i.e. the time scale on which the fluid reaches the steady state in response to an instantaneous change in the driving pressure. A critical Womersley number α_c for a circular tube may then be defined as

$$\alpha_c \equiv \sqrt{\frac{a^2}{\gamma_1^2\,\nu}\,\omega} = \sqrt{\tau\omega} = \frac{\alpha}{\gamma_1}, \tag{2}$$

which then measures the fluid relaxation time in response to the rate of change of the pressure ω. It is immediately seen that for $\alpha_c < 1$ the fluid at all times reaches a steady state before changes happen to the pressure, and the fluid flow is quasi-steady. For $\alpha_c > 1$ the fluid does not reach a steady state before the pressure changes, and inertia becomes important. Snapshots of the velocity profile computed using MATLAB are given in figure 1. The steady-state Poiseuille paraboloid is retrieved in the quasi-steady limit ($\alpha_c = 1/5$, panel (a)), while for $\alpha_c > 1$ (panels (c) and (d)) increasingly more pronounced deviations from this are seen as the flow becomes increasingly more dominated by inertia.

For $\alpha_c > 1$ the flow still has inertia acting in the opposite direction when the pressure gradient is reversed. Consequently, it will take some time before the pressure

gradient can change the direction of the inertia. This introduces a phase shift between the fluid motion and the pressure gradient. However, at the confinement walls, the no-slip boundary condition enforces very low velocities with correspondingly low inertia, so fluid close to the walls have a smaller phase shift than fluid in the center of the confinement. At $\alpha_c \gtrsim 5$ a full π phase shift is observed between the flow close to the walls and that at the center, forming a 'fluidic skin effect' or annular region as documented experimentally by Richardson [26]. The width of this region is given by the momentum diffusion length λ_d which can be found from the diffusivity of momentum and the characteristic time ω^{-1} as $\lambda_d = \sqrt{\nu/\omega}$. The parabolic velocity profile in this annular region observable in figure 1(*d*) supports the notion that the flow here remains quasi-static for $\alpha_c > 1$.

As previously shown by Morris and Forster [6], one may derive an exact fluidic impedance Z_{hyd} from Womersley's analytical solution accounting for both inertia and viscous resistance. It relates pressure and flow rate amplitudes as $\Delta \tilde{p} = Z_{\mathrm{hyd}} \tilde{Q}$ with

$$ Z_{\mathrm{hyd}} = \frac{\rho \omega \ell}{\pi a^2} i \left[1 - \frac{2 J_1\left(\alpha \, i^{\frac{3}{2}}\right)}{\alpha \, i^{\frac{3}{2}} \, J_0\left(\alpha \, i^{\frac{3}{2}}\right)} \right]^{-1}, \qquad (3) $$

where J_n is the Bessel function of the first kind of order n, t is the time and $i = \sqrt{-1}$.

The field of pulsatile microfluidics is largely unexplored and has previously only been used in the study of reciprocating pumps. Olsson *et al* [2] correctly assumed a plug-flow velocity profile in the pump chamber without justifying the assumption. In an experimental study, Sheen *et al* [27] assumed a parabolic velocity profile even though their results extended into the inertially dominated regime where this assumption becomes invalid. One correct treatment of the fluid physics into this regime in connection with micropumps is given by Morris and Forster [6].

2.1. Resistance of pulsatile flow

The hydraulic resistance of a pressure-driven flow is a result of the conversion of kinetic energy into heat through viscous power dissipation P. For a fully developed flow in a tube of circular cross section of radius a and axial length ℓ it is given by [8]

$$ P = \eta \, 2\pi \, \ell \int_0^a r [\partial_r v_x(r)]^2 \, \mathrm{d}r, \qquad (4) $$

where v_x is the axial velocity. In the quasi-steady limit the resistance does not differ from that of Poiseuille flow, but deviations appear in the limit of $\alpha_c > 1$ since the velocity profile gradient changes. These changes are observable in figure 1. The velocity amplitude $\tilde{v}_x$ scales as the acceleration times the characteristic time, where the former is force per mass $\mathcal{A}\Delta \tilde{p} / (\rho \mathcal{A} \ell)$ and the latter is ω^{-1}, so $\tilde{v}_x \propto \Delta \tilde{p} / \omega$. The integrand $\partial_r v_x \approx \tilde{v}_x / \lambda_d$ differs only significantly from zero within a small annulus of radius a and width $\lambda_d = \sqrt{\nu/\omega}$ so the viscous power dissipation can be estimated as

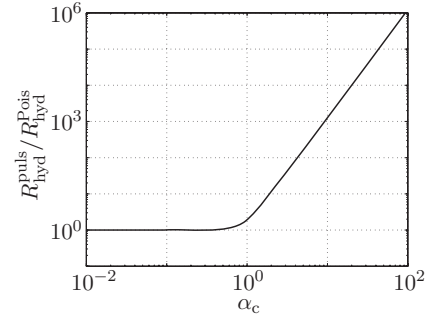$$ P \propto 2\pi \, a \, \lambda_d \frac{\tilde{v}_x^2}{\lambda_d^2} \propto \Delta \tilde{p}^2 \omega^{-\frac{3}{2}}. \qquad (5) $$

Figure 2. Model calculation of the time-averaged resistance of the pulsatile flow $R_{\mathrm{hyd}}^{\mathrm{puls}}$ normalized by the resistance of the Poiseuille flow $R_{\mathrm{hyd}}^{\mathrm{Pois}}$, plotted as a function of the critical Womersley number α_c. A sharp increase is observed when the flow enters the inertially dominated regime of $\alpha_c \geqslant 1$, where $R_{\mathrm{hyd}}^{\mathrm{puls}} \propto \alpha_c^3$.

For Poiseuille flow one finds $R_{\mathrm{hyd}}^{\mathrm{Pois}} = 8\eta \ell / (\pi a^4) = (\Delta \tilde{p})^2 / P$, so the hydraulic resistance of the pulsatile flow scales as $R_{\mathrm{hyd}}^{\mathrm{puls}} \propto \omega^{\frac{3}{2}} \propto \alpha_c^3$ for high α_c.

This remarkable estimate may be verified from the impedance of equation (3) by considering the time-averaged resistance of the pulsatile flow over one oscillation cycle. The time-averaged power consumption is $\langle P \rangle = \mathrm{Re}[\tilde{Q}^* \Delta \tilde{p}]/2$, where Re and the asterisk indicates the real part and the complex conjugate, respectively. Choosing the pressure amplitude to be real and defining all phases relative to $\Delta \tilde{p}$ while noting that $\tilde{Q} = \Delta \tilde{p}/Z_{\mathrm{hyd}}$ we find

$$ \langle P \rangle = \frac{1}{2}\mathrm{Re}\left[\frac{1}{Z_{\mathrm{hyd}}}\right] \Delta \tilde{p}^2. \qquad (6) $$

To correctly compare to a Poiseuille flow, the same pressure difference must be used. By direct analogy to voltage in ac electric systems we find $\Delta p_{\mathrm{rms}} = \Delta \tilde{p}/\sqrt{2}$ yielding $P = \Delta \tilde{p}^2 / (2 R_{\mathrm{hyd}})$, so comparing to equation (6) we then find the time-averaged resistance of the pulsatile flow to

$$ R_{\mathrm{hyd}}^{\mathrm{puls}} = \frac{1}{\mathrm{Re}\left[\frac{1}{Z_{\mathrm{hyd}}}\right]}, \qquad (7) $$

which exhibits the suggested dependence on α_c^3, as shown in figure 2 or as seen from equation (3). This result emphasizes the need to use the correct impedance of equation (3) when modeling the pulsatile flow.

3. Pressure source

A thorough survey of micropumps and flow generators, both commercially available and documented in the scientific literature [28, 29], shows that few which operate up to the low-kilohertz range generate very small flow rates. To satisfy the criterion of stroke volumes of $\mathcal{V} \sim 0.1$ mm^3 we have developed a novel pressure source to better probe the desired frequency range.
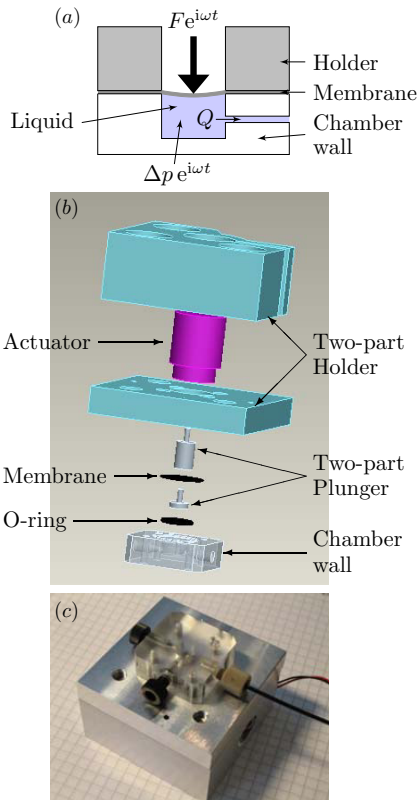
Figure 3. The constructed pressure source. (*a*) Sketch of the working principle. (*b*) 3D CAD drawing. (*c*) The assembled pressure source shown upside-down on a piece of paper with grid lines intersecting every 5 mm.

Figure 4. (*a*) Example of experimentally measured performance of the pressure source at $f = 10$ Hz. The generated pressure p (full line) is clearly pulsatile in response to the applied harmonically oscillating electric current I (dashed line). (*b*) Experimentally determined (full line) and model predictions (dashed line, see section 3.2) of the pressure amplitude Δp as a function of oscillation frequency f for current amplitude of 1.0 A. The experimental data indicate a resonance around $f = 350$ Hz, which the model predicts to be $f = 340$ Hz. The discrepancy between the model results and the experimental data for high frequencies can be explained by the simplifying assumption that the actuator membrane acts as a linear spring (see equation (8)). It is likely that the membrane does in fact exhibit a viscoelastic behavior which would account for the large value of the experimentally observed damping.

3.1. Design and fabrication

The pressure source works by applying a harmonically oscillating linear force onto a liquid-filled chamber, see figure 3(*a*). A linear actuator is used to deliver the force onto a silicone rubber membrane via a plunger, with the membrane separating the liquid system from the surroundings.

A linear voice coil actuator (LA08-10-000A by BEI Kimco Magnetics, San Marcos, CA, USA) was used as the driving mechanism. By virtue of the Lorentz force, this actuator delivers a linear force in response to an electric current in the coil, and it can probe frequencies of up to $f = 0.99$ kHz while still delivering stroke volumes of $\mathcal{V} \sim 0.1$ mm^3. Power was delivered to the actuator from an electric ac generator.

An aluminum holder is used to fixate the actuator and consists of two parts which are held together by screws. A two-part titanium plunger is fastened into the actuator coil. The membrane is clamped between the two parts of the plunger thereby forcing the thin silicone rubber membrane (0.20 mm thickness) to follow the motion of the plunger during the entire oscillation cycle. To ensure a complete sealing of the liquid in the chamber, the membrane is also clamped between the bottom part of the holder and the chamber wall, with a small rubber *O*-ring placed in a groove around the edge of the chamber. The chamber (4.50 mm radius and 6.50 mm depth) has three threaded holes for connection to the fluid system. The chamber wall is mounted onto the actuator holder by four
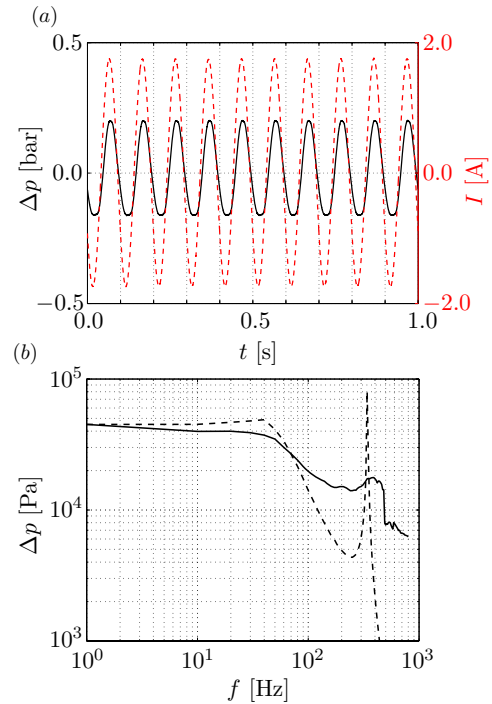
screws. An exploded 3D CAD drawing of the pressure source is given in figure 3(*b*), while the assembled source is shown in panel (*c*).

The performance of the pressure source is illustrated in figure 4. Panel (*a*) shows that the pressure source does in fact deliver a pulsatile pressure when operated with a 10 Hz harmonically oscillating electric current, while panel (*b*) indicates the attainable pressure amplitude as a function of frequency for a current amplitude of 1.0 A. The capability of the source is thus demonstrated to deliver pressures in the kPa range up to at least $f = 0.8$ kHz, the largest applied frequency in the measurement.

3.2. Pressure source circuit model

In order to couple the pressure source to the EC equations for the microfluidics of the system it acts on, a simple circuit model has been developed to account for the coupled electric, mechanical and microfluidic physics governing the pressure source. Assuming that all fields vary harmonically in time as $g(t) = \tilde{g}\, e^{i\omega t}$, the derivatives with respect to time simplify as
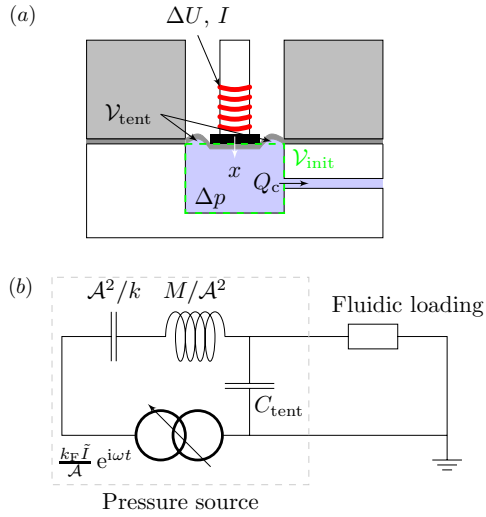
Figure 5. (*a*) Schematic illustration of the pressure source indicating the coil voltage ΔU and current I, the initial chamber volume $\mathcal{V}_{init}$ and membrane 'tent' volume $\mathcal{V}_{tent}$, as well as the fluidic responses: pressure Δp and the chamber flow rate Q_c.
(*b*) Equivalent circuit diagram for the pressure source with a plunger of mass M and area $\mathcal{A}$, a membrane of stiffness k and compliance C_{tent}, and the coil of current amplitude $\tilde{I}$ and back-EMF constant k_F. The fluidic loading is determined by the system the source acts on.

$\partial_t \rightarrow i\omega$. A schematic representation of the pressure source is given in figure 5(*a*).

The motion of the coil is governed by Newton's second law, where the external forces are the electromagnetic force on the actuator $F_{act} = k_F I(t)$, the assumed linear spring force of the membrane $F_m = -kx(t)$, and the force arising when a pressure difference exists across the membrane $F_p = -\mathcal{A}\Delta p(t)$, where $\mathcal{A}$ is the effective area the plunger acts on. The motion of the plunger of mass M is then given by

$$-M\omega^2 \tilde{x} = k_F \tilde{I} - k\tilde{x} - \mathcal{A}\Delta\tilde{p}, \tag{8}$$

where $\tilde{x}$ is the plunger displacement amplitude, and the coil velocity $\tilde{v}_{coil}$ is found as

$$\tilde{v}_{coil} = i\omega\tilde{x}. \tag{9}$$

The coil electric circuit obeys the equation

$$\Delta\tilde{U} = R_{el}\tilde{I} + i\omega L_{el}\tilde{I} + k_F\tilde{v}_{coil}, \tag{10}$$

where k_F is the back-EMF constant.

During operation, the volume of the chamber $\mathcal{V}_c$ depends on the position of the plunger and the expansion of the membrane due to the generated over-pressure in the chamber. The plunger radius is 3.53 mm while the chamber radius is 4.50 mm, so a small free-membrane area exists between the plunger and the chamber and holder walls. This part of the membrane will expand when a pressure difference is present across it due to its elastic nature, and the expanded volume will be filled with incoming fluid. Denoting the volume of fluid stored in the expanded membrane $\mathcal{V}_{tent}$—so named due to the resemblance of the expanded membrane to a tent—and noting that the volume displaced by the actuator is $\mathcal{V}_{disp}(t) = \mathcal{A}x(t)$, the chamber volume is given by

$$\mathcal{V}_c = \mathcal{V}_{tent} - \mathcal{A}x(t) + \mathcal{V}_{init}. \tag{11}$$

$\mathcal{V}_{init}$ is the volume of the chamber when the system is at rest, and the negative sign arises since a positive displacement of the plunger pushes liquid out of the chamber. The volume $\mathcal{V}_{tent}$ is related to the generated over-pressure through a compliance as

$$\mathcal{V}_{tent} = C_{tent}\Delta p(t). \tag{12}$$

A positive flow rate Q_c exits the chamber when its volume is diminished, so this flow rate is found as the negative time rate of change of equation (11):

$$\tilde{Q}_c = \mathcal{A}\tilde{v}_{coil} - i\omega C_{tent}\Delta\tilde{p}. \tag{13}$$

Equations (8)–(10) and (13) couple the six unknown amplitudes $\tilde{x}$, $\tilde{v}_{coil}$, $\Delta\tilde{U}$, $\tilde{I}$, $\Delta\tilde{p}$ and $\tilde{Q}_c$, so two additional equations are required to close the system. These are derived from the 'fluidic loading' on the source, i.e. expressions for the flow rate and total pressure difference of the system driven by the source. However, the following equation relating the generated flow rate and over-pressure may be deduced from equations (8), (9) and (13):

$$\tilde{Q}_c = \frac{k_F\tilde{I}}{\mathcal{A}\left(\frac{k}{\mathcal{A}^2}\frac{1}{i\omega} + \frac{M}{\mathcal{A}^2}i\omega\right)}$$
$$- \Delta\tilde{p}\left[\left(\frac{k}{\mathcal{A}^2}\frac{1}{i\omega} + \frac{M}{\mathcal{A}^2}i\omega\right)i\omega C_{tent} + 1\right]. \tag{14}$$

An expression for the pressure amplitude as a function of the electric current amplitude and plunger velocity can also be derived from equations (8) and (13):

$$\Delta\tilde{p} = \frac{k_F\tilde{I}}{\mathcal{A}} - \left(\frac{k}{\mathcal{A}^2}\frac{1}{i\omega} + \frac{M}{\mathcal{A}^2}i\omega\right)\tilde{v}_{coil}\mathcal{A}. \tag{15}$$

Equations (14) and (15) reveal that the pressure source does deliver a pressure, which can maximally be $\Delta p_{max} = k_F\tilde{I}/\mathcal{A}$. However, not all of the actuator force is deposited as pressure in the fluid, as some is used to accelerate the plunger and membrane. These time-dependent losses are observed to enter the fluid equations as a hydraulic inertance $M/\mathcal{A}^2$ and compliance $\mathcal{A}^2/k$, which are both given in terms of the known quantities M, k and $\mathcal{A}$. This compliance is a consequence of the spring behavior of the membrane, which arises because some of the coil force is required to elongate the membrane. Hence, the flow rate leaving the chamber is less than what would have been the case if no force were required to deflect the membrane. This, in the view of the microfluidics, is the same as a storage of volume inside the chamber, and it is therefore not surprising to find the membrane elasticity enter into the equations as another compliance in addition to C_{tent}.

The circuit diagram for the EC model of the pressure source is given in figure 5(*b*), and table 2 lists the values of the physical parameters. The membrane spring constant k was determined experimentally by fitting the model results to the experimental data in figure 4(*b*), and fair agreement is found. However, the width of the resonance peak in the experimental data around 350 Hz and the weak amplitude decrease above 50 Hz are not well reproduced by the model. These deviations can be explained by the simplifying assumption that the actuator membrane acts as a Hookean spring, but it is likely that it does in fact display a viscoelastic behavior, which would account for the large value of the observed damping.
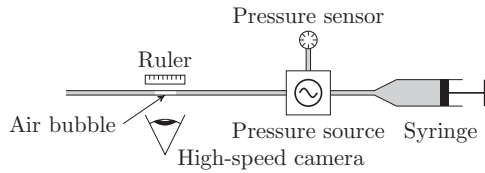
Figure 6. Schematic illustration of the experimental setup used for the proof of concept experiment.

Table 2. Physical parameters for the pressure source circuit model.

Symbol	Value
$\mathcal{A}$	7.61×10^{-5} m^2
C_{tent}	2.0×10^{-13} m^3 Pa^{-1}
k	1.1×10^4 N m^{-1}
k_{F}	2.7 V s m^{-1}
L_{el}	2.1×10^{-4} H
M	8.64×10^{-3} kg
R_{el}	$2.4 \, \Omega$

4. Experimental considerations

The proposed method is generic and thus applies to all systems exhibiting temporal dependence. For illustration, we study in the following the fairly complex physical system of a full water-filled system of interconnected elastic microfluidic tubes with a trapped air bubble driven by a pulsatile pressure difference. A schematic drawing of the system is given in figure 6. We will compare the experimental results to the predictions of a system-level EC model, with one unknown parameter, see section 7. We emphasize that even though the proof of concept study presented here involves an ac system, no such limitations apply to the method of using the pulsatile pressure source to deduce the time scales of a system.

The motion of gas bubbles in liquids has been studied extensively in the literature, see e.g. [30–35], but very few accounts using the EC approach have been found, e.g. Fuerstman *et al* [36].

4.1. Setup and method

A schematic illustration of the setup is shown in figure 6. A differential pressure sensor (Honeywell 40PC by Honeywell International Ltd, Morristown, NJ, USA) was connected to one of the three chamber outlets through a teflon tube ($\ell_{\text{sen}} = 4.1$ cm, $a_{\text{sen}} = 0.125$ mm, $h_{\text{sen}} = 0.669$ mm) and a milli-Q water-filled 10 mL syringe (filled to 8.1 mL) to another of the outlets via a teflon tube of dimensions $\ell_{\text{syr}} = 17.5$ cm, $a_{\text{syr}} = 0.125$ mm and $h_{\text{syr}} = 0.669$ mm. A long transparent tube ($\ell = 42.9$ cm, $a = 0.254$ mm, $h = 0.540$ mm) was connected to the last chamber outlet, allowing the tube to exit into an open reservoir. The bubble (relaxed axial length $\ell_{\text{bub}} = 1.35$ cm) was placed in this tube, roughly halfway between the chamber and the tube outlet. A metric ruler was placed next to the tube and just above the bubble for scale.

The bubble motion was detected using a Photron Fastcam APX RS high-speed camera (Photron USA Inc., San Diego,
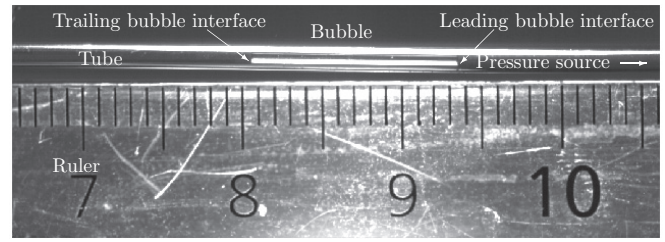

Figure 7. Example of a raw bubble image from the camera showing part of the tube exiting the pressure source chamber. The right end of the tube is connected to the pressure source while the left end exits into atmospheric conditions. The bubble is found roughly in the middle of the tube. A mm-scale ruler (numbers indicate centimeter) is positioned below the tube for scale.

CA, USA) fitted with a 1:2.8D lens (AF Micro Nikkor by Nikon Corp., Imaging Company, Tokyo, Japan), with dedicated Photron software used for storage. Individual gray scale images were framed at 1 kHz sampling rate and stored in `tiff` format, for a time interval comprising several oscillation periods. An example of an image is given in figure 7, where the pressure source found to the right of the photo. The bubble interface closest to the pressure source—the right-most interface in the photo—is termed the 'leading interface' while the interface the furthest away from the source is referred to as the 'trailing bubble interface'.

The bubble position was adjusted using the syringe. Once in place and with a specified pressure frequency, the ac generator and camera were activated simultaneously. Images were taken for 6 s, after which the supply voltage to the pressure source was turned off. The experiment was conducted at the frequencies of 1 Hz, 30 Hz, 50 Hz and 100 Hz, and for each experiment, the pressure and the electric current driving the actuator were recorded.

4.2. Image processing

An image-processing routine has been developed in MATLAB to deduce the motion of the air–water interfaces of the bubble. Upon loading the raw `tiff` image and converting it to black/white (represented as 0 and 1, respectively), the routine searches for the first white pixel in a specified region by searching for the first pixel with value above 0.5. This first pixel of the bubble is approximately the position of the boundary. The position of this pixel is stored and the routine continues to the next image in the set. This analysis is done for both left and right bubble interface, and the positions of both interfaces are plotted versus time. A scale is found as the horizontal distance between 2 mm marks on the ruler in the first image of the set.

5. Experimental results

A bubble-relative reference frame, denoted by a subscript 'rel', is placed with the x-axis along the axis of the tube and with the origin at the bubble equilibrium position. The motion of the two bubble interfaces about this equilibrium position as
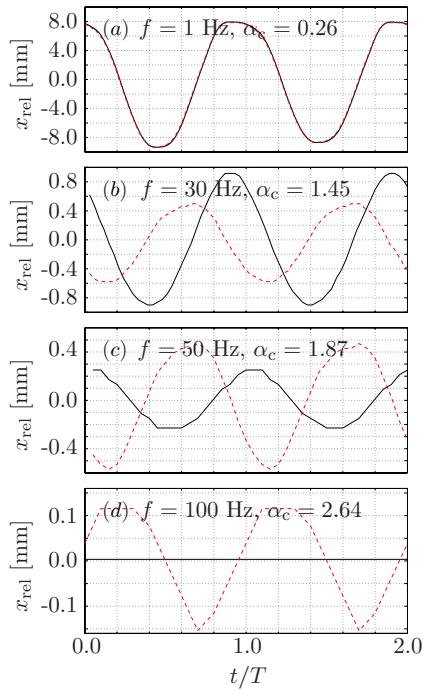
Figure 8. The measured motion of the leading (dashed line) and trailing (full line) air bubble boundaries about an equilibrium position as picked out by the image-processing routine at four different frequencies. The time axis has been normalized by the oscillation period T. Resistance dominates the pulsatile flow of liquid for $\alpha_c < 1$ while inertia dominates for $\alpha_c > 1$. The resonance indicated by the data is likely caused by the interplay of the compliance of the bubble and the inertia of the liquid.

picked out by the image-processing routine is given in figure 8 for all four frequencies. The critical Womersley number for the milli-Q water is given for all frequencies and it is observed that inertia dominates the water for all but the case of 1 Hz since $\alpha_c > 1$ for the former and $\alpha_c < 1$ for the latter.

The motion of both interfaces is approximately sinusoidal in the entire frequency range, and clearly so at the intermediate frequencies of $f = 30$ Hz and $f = 50$ Hz. The deviations at $f = 1$ Hz may be attributed to the fact that the plunger displacement at this frequency vastly exceeds the displacements at the following frequencies, so the assumed linear spring behavior of the membrane is no longer valid. At $f = 100$ Hz noticeable pixelation makes it somewhat difficult to see the sinusoidal motion of the interfaces.

The two interfaces move completely in phase at $f = 1$ Hz (hence the dashed line cannot be seen), but shifts in both phase and amplitude are found for all subsequent frequencies. At 30 Hz the trailing bubble interface has a larger amplitude than the leading interface, which is reversed at 50 Hz. At $f = 100$ Hz there is no motion of the trailing bubble interface. This sudden increase followed by a rapid decrease in amplitude coupled with a simultaneous change in phase lag from 0 through $\pi/2$ to π indicates a resonance near 30 Hz.

The pressure source stroke volumes can also be verified deduced from this simple experiment. The displacement of the air bubble ℓ_{disp} in either direction about its equilibrium position is due to the displacement of liquid. Thus, the stroke

Table 3. Elastic wave speeds for common tube materials used in experimental microfluidics, and stainless steel for comparison.

Material	Young's modulus (GPa)	Wave speed (m s^{-1})
Silicone rubber	0.002	1.75×10^2
Teflon	0.50	9.41×10^2
PEEK	3.60	2.38×10^3
Stainless steel	210	6.04×10^3

volume is $\mathcal{V} = \ell_{disp}\pi a_{bub}^2$. With $a_{bub} = 0.254$ mm, the stroke volume varies from about 2 mm^3 at $f = 1$ Hz to ~ 0.03 mm^3 at $f = 100$ Hz. The stroke volume is above or close to the desired 0.1 mm^3 during the entire probed interval, and higher volumes can easily be achieved by increasing the electric power to the actuator.

5.1. EC interpretation of the observations

To interpret the observed resonance frequency at $f = 30$ Hz, the physical system of the bubble in the long, water-filled tube is analyzed as an electric RCL-circuit. Since inertia in the liquid dominates at 30 Hz ($\alpha_c = 1.45$) the observed resonance is believed to be of the LC-type with the dominating compliance stemming from the bubble. Using the regular expressions for inertance $L_{hyd} = \rho\ell/(\pi a^2)$ and isothermal compliance of an air bubble $C_{hyd} = \mathcal{V}_0/p_0$ [8] where the subscript '0' indicates a reference state and $\mathcal{V}_0 = \ell_{bub}\pi a_{bub}^2$, we find

$$f = \frac{1}{2\pi\sqrt{L_{hyd}C_{bub}}} = 30.86 \text{ Hz}. \qquad (16)$$

This is in good agreement with the experimental observation of $f \approx 30$ Hz, so the resonance is likely caused by the interplay of liquid inertia and bubble compliance. Also, this simple analysis indicates the strength of EC modeling in predicting system dynamics.

6. Compliance of elastic tubing

The system under consideration consists of interconnected elastic tubes of the circular cross section with sub-millimeter inner radius. To account for all temporal effects of the system in a system-level EC model, an expression for this elastic tube wall compliance is needed. This may be derived from the definition of compliance $C_{hyd} = d\mathcal{V}/dp$ [8], and the elastodynamic equation, see e.g. [37]. Under the assumption of radial displacements only, the elastic wave speeds of the wall displacements for common tube materials from experimental microfluidics are listed in table 3 based on data from [38, 39]. A typical tube has the wall thickness $h \sim 0.5$ mm, so changes in the pressure inside the tube will traverse the wall in $t \sim 3$ µs for a silicone rubber tube, and faster for all other materials listed due to their higher wave speeds, so the wall can be considered quasi-static even for pressure oscillations in the kilohertz regime.
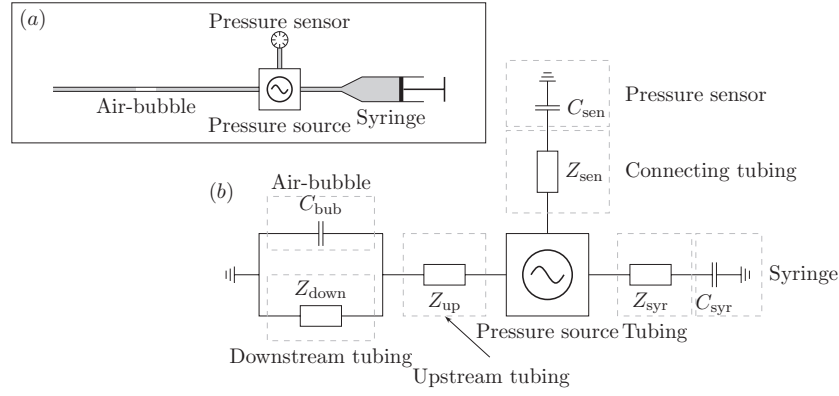
Figure 9. System-level EC model for the experiment. (*a*) The schematic representation of the setup shown for convenience. (*b*) The EC model of the full system.

The steady state tube wall displacement is [37]

$$u_r(r) = (1 + \sigma)\left[(1 - \sigma) + \frac{(a+h)^2}{r^2}\right]\frac{a^2}{(a+h)^2 - a^2}\frac{p}{E}r,$$

(17)

where E is Young's modulus and σ is Poisson's ratio. The volume increase associated with the displaced wall is $\mathcal{V} = 2\pi a \ell u_r(a)$. The compliance is then found as

$$C_{\text{hyd}} = \beta\frac{2\pi a^3\ell}{Eh},$$

(18)

with the non-dimensional constant β given by

$$\beta = \frac{a}{h+2a}(1+\sigma)\left[2(1-\sigma) + 2\frac{h}{a} + \frac{h^2}{a^2}\right].$$

(19)

The compliance of equation (18) applies to all anisotropic materials of all wall thicknesses. In the limit $h \ll a$ we find $\beta \approx 1 - \sigma^2$ with $\sigma^2 \approx 0$ since $0 \leqslant \sigma \leqslant 0.5$, so the wall compliance becomes $C_{\text{hyd}} = 2\pi a^3\ell/(Eh)$. This is a well-known result used in several cases to model the arterial wall [40–44]. In the other limit of $h \gg a$, usually found in experimental microfluidics, the compliance becomes $C_{\text{hyd}} = 2\pi a^2\ell(1+\sigma)/E$, which is independent of the wall thickness h.

A typical teflon tube segment has the dimensions $\ell \sim 10^2$ mm, $h \sim 0.5$ mm and $a \sim 0.2$ mm, and since the Poisson ratio is $\sigma = 0.45$ the compliance of the tube is $C_{\text{hyd}} \sim 3 \times 10^{-17}$ m^3 Pa^{-1}. The air bubble for this experiment has the rest volume $\mathcal{V}_0 = \ell_{\text{bub}}\pi a_{\text{bub}}^2$ which is $\mathcal{V}_{\text{bub}} \sim 3$ mm^3 since $a_{\text{bub}} = 0.254$ mm, and the experiment was done at standard atmospheric conditions, so $p_0 \sim 10^5$ Pa. The compliance of this air bubble is then $C_{\text{hyd}} \sim 3 \times 10^{-14}$ m^3 Pa^{-1}, which is three orders of magnitude greater than the compliance of the elastic wall. This latter may therefore be neglected when modeling the experiment.

7. System-level EC model

The full system-level model is summarized in figure 9, where the elastic walls have been neglected as just described. The numerical values of the circuit elements are easily obtained from equation (3) and $C_{\text{hyd}} = p_0/\mathcal{V}_0$, but the compliance of

Table 4. Values for the EC elements of the model of the full system at $f = 1$ Hz.

Element	Value
C_{bub}	2.70×10^{-14} m^3 Pa^{-1}
C_{syr}	3.61×10^{-13} m^3 Pa^{-1}
Z_{down}	$1.23 \times 10^{12} + \text{i}\,8.26 \times 10^9$ Pa s m^{-3}
Z_{sen}	$6.80 \times 10^{11} + \text{i}\,1.11 \times 10^{11}$ Pa s m^{-3}
Z_{syr}	$1.83 \times 10^{12} + \text{i}\,2.98 \times 10^{10}$ Pa s m^{-3}
Z_{up}	$1.36 \times 10^{12} + \text{i}\,8.86 \times 10^9$ Pa s m^{-3}

the pressure sensor is difficult to determine from theoretical considerations. This compliance arises since the senor detects pressure through the deflection of a silicon membrane. Hence, we choose to determine this compliance from the experiment by measuring both pressure in the sensor and actuator electric current, and fitting C_{sen}. In turn, this approach proves the applicability of the method to any undetermined compliance in a microfluidic system.

The syringe is connected to the pressure source chamber using the same teflon tubing as for the pressure sensor. In theory, the connecting tubing and the syringe should each be modeled using individual impedances and compliances; however, the syringe itself has a much larger radius than the tubing, so the syringe impedance may be neglected to a good approximation since $Z_{\text{hyd}} \propto a^{-2}$, but its compliance cannot since C_{hyd} of equation (18) depends on a^3.

The imaged bubble is modeled as previously mentioned with $C_{\text{bub}} = \mathcal{V}_0/p_0$ using $\mathcal{V}_0 = \ell_{\text{bub}}\pi a_{\text{bub}}^2$ for simplicity, although the axial length of the bubble is observed to change during experimentation for 30 Hz and 50 Hz. Given the level of approximation otherwise employed the deviations introduced by this simplification are negligible. The values of the circuit elements for $f = 1$ Hz are listed in table 4; the impedances of course change as they are frequency dependent.

The motion of the bubble interfaces are derived from the flow rates up and downstream of the bubble by noting that the volume and flow rate are related as $\mathcal{V} = \int Q(t)\,\text{d}t$ with $\mathcal{V} = x_{\text{rel}}\pi a^2$ using x_{rel} of section 5. The bubble-interface displacement amplitudes $x_{\text{rel}}^{\text{LI}}$ (leading interface) and $x_{\text{rel}}^{\text{TI}}$ (trailing interface) are given in terms of the applied electric
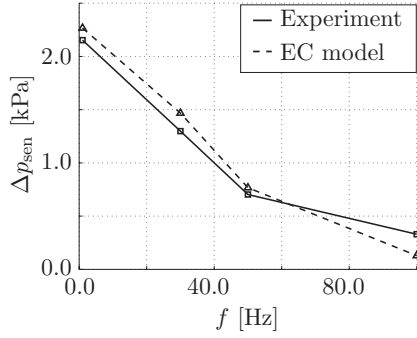
Figure 10. Sensor pressure difference used for determining the correct value of the sensor compliance by comparison of experimental and system-level EC model results. The figure shows the best fit which is found for the value $C_{\text{sen}} = 2.50 \times 10^{-14}$ m^3 Pa^{-1}.

current amplitude $\tilde{I}$ by

$$\tilde{x}_{\text{rel}}^{\text{LI}} = \frac{\frac{k}{\mathrm{i}\omega\mathcal{A}^2} + \mathrm{i}\omega\frac{M}{\mathcal{A}^2}}{Z_{\text{tot}}} \frac{1}{\mathrm{i}\omega\pi a_{\text{bub}}^2} \frac{1}{Z_{\text{up}}} \frac{k_{\text{F}}\tilde{I}}{\mathcal{A}}, \tag{20}$$

$$\tilde{x}_{\text{rel}}^{\text{TI}} = \frac{\frac{k}{\mathrm{i}\omega\mathcal{A}^2} + \mathrm{i}\omega\frac{M}{\mathcal{A}^2}}{Z_{\text{tot}}} \frac{1}{\mathrm{i}\omega\pi a_{\text{bub}}^2}$$
$$\times \frac{1}{Z_{\text{down}} + Z_{\text{up}} + \mathrm{i}\omega C_{\text{bub}} Z_{\text{down}} Z_{\text{up}}} \frac{k_{\text{F}}\tilde{I}}{\mathcal{A}}, \tag{21}$$

where the total system impedance Z_{tot} is

$$Z_{\text{tot}} = \frac{k}{\mathrm{i}\omega\mathcal{A}^2} + \mathrm{i}\omega\frac{M}{\mathcal{A}^2} + \big\{\mathrm{i}\omega C_{\text{tent}}$$
$$+ [Z_{\text{syr}} + (\mathrm{i}\omega C_{\text{syr}})^{-1}]^{-1} + [Z_{\text{sen}} + (\mathrm{i}\omega C_{\text{sen}})^{-1}]^{-1}$$
$$+ \big[Z_{\text{up}} + \big(\mathrm{i}\omega C_{\text{bub}} + Z_{\text{down}}^{-1}\big)^{-1}\big]^{-1}\big\}^{-1}. \tag{22}$$

8. Comparison of system-level EC model and experiment

In order to compare the model and experimental results, the undetermined value of the pressure sensor compliance is first determined as follows: the pressure in the sensor is computed from the system-level model using the measured electric coil current as input, and then compared to the measured pressure in the same location. C_{sen} is tuned until the best agreement between experimental and model data is found at all probed frequencies, which turns out to be for $C_{\text{sen}} = 2.50 \times 10^{-14}$ m^3 Pa^{-1}, see figure 10.

The results of the system-level EC model, given in figure 11, shows that the model correctly predicts the observed dynamics for all probed frequencies, while also giving the correct amplitudes and phase shift between the leading and trailing interfaces. The complex microfluidic system can thus be adequately modeled by EC theory.

The model captures the amplitudes of the oscillations of the leading interface better than the trailing interface, with some of the discrepancy at 1 Hz and 30 Hz attributed to the assumption of constant bubble length in the model although the experimental data suggests otherwise. The resolution of the images is 40.0 µm per pixel, so the discrepancy of
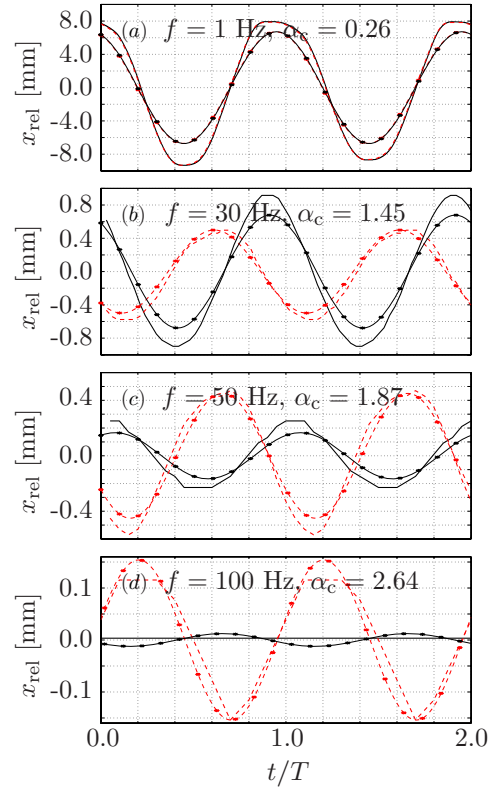

Figure 11. Comparison of experimental and model results for the motion of the leading (dashed) and trailing (solid) air bubble interfaces at four frequencies. The time axis is normalized by the oscillation period T. The experimental results (thick lines) and model results (thin and starred lines) show very good agreement for all four frequencies.

the trailing interface at 100 Hz is below this threshold and the motion predicted by the model cannot be ruled out. Furthermore, the existence of a resonance around 30 Hz observed experimentally and further suggested from the simplest circuit analysis is also captured by the system-level model.

9. Concluding remarks

In conclusion, we have proposed the use of pulsatile microfluidics as an analytical tool leading to understanding and determination of the transient time scales of any microfluidic system. A novel pressure source has been fabricated and tested. It resolves the appropriate frequency range for most such systems, while still delivering stroke volumes of $\mathcal{V} \sim 0.1$ mm^3.

As a proof of concept, pulsatile kilohertz microfluidics has been applied to a full system of interconnected and milli-Q water-filled elastic tubes of sub-millimeter radius containing a trapped air bubble, and good agreement between an equivalent circuit theory model and the experimental results have been found. Moreover, the predictive capabilities of the equivalent circuit model have been demonstrated by deducing an unknown compliance from the comparison of model results and experimental data.

Although the method suggested in this paper is directly analogous to the approaches of experimental electric circuit analysis, its realization is substantially more cumbersome. This is due to the scaling of fluid inertia and the (unexpected) scaling of fluid resistance with driving frequency, which combine to make pulsatile microfluidics into the low-kilohertz range with stroke volumes of $\mathcal{V} \sim 0.1$ mm^3 very difficult to produce. However, the prospect of microfluidic systems with application-tuned dynamic time scales and the just mentioned difficulties of experimentally conducting system-level circuit analysis only emphasize the need for analytical tools like the one presented here.

Acknowledgments

References

[1] Thorsen T, Maerkl S and Quake S R 2002 *Science* **298** 580
[2] Olsson A, Stemme G and Stemme E 1999 *J. Micromech. Microeng.* **9** 34
[3] Brask A, Snackenborg D, Kutter J P and Bruus H 2006 *Lab Chip* **6** 280
[4] Leslie D L, Easley C J, Seker E, Karlinsey J M, Utz M, Begley M R and Landers J P 2009 *Nat. Phys.* **5** 231
[5] Mortensen N A and Bruus H 2006 *Phys. Rev.* E **74** 017301
[6] Morris C J and Forster F K 2004 *Exp. Fluids* **36** 928
[7] Bourouina T and Grandchamp J-P 1996 *J. Micromech. Microeng.* **6** 398
[8] Bruus H 2008 *Theoretical Microfluidics* (Oxford: Oxford University Press)
[9] Kim D, Chesler N C and Beebe D J 2006 *Lab Chip* **6** 639
[10] Zengerle R and Richter M 1994 *J. Micromech. Microeng.* **4** 192
[11] Brask A, Goranović G and Bruus H 2003 *Sensors Actuators B* **92** 127
[12] Vedel S 2009 *Master's Thesis* Technical University of Denmark available online at www.nanotech.dtu.dk/microfluidics
[13] Geng X, Yuan H, Oğuz H N and Prosperetti A 2001 *J. Micromech. Microeng.* **11** 270
[14] Tsai J H and Lin L 2002 *J. Microelectromech. Syst.* **11** 665
[15] van der Wijngaart W, Chugh D, Man E, Melin J and Stemme G 2007 *J. Microelectromech. Syst.* **16** 765
[16] Xu W, Wu L L, Zhang Y, Xue H, Li G P and Bachman M 2009 *Sensors Actuators B* **142** 355
[17] de Jong J, de Bruin G, Reinten H, van der Berg M, Wijshoff H, Versluis M and Lohse D 2006 *J. Acoust. Soc. Am.* **120** 1257
[18] Satoh W, Shimizu Y, Kaneto T and Suzuki H 2006 *Sensors Actuators B* **123** 1153
[19] Maxwell R B, Gerhardt A L, Toner M, Gray M L and Schmidt M A 2003 *J. Microelectromech. Syst.* **12** 630
[20] Hua S Z, Sachs F, Yang D X and Chopra H P 2002 *Anal. Chem.* **74** 6392
[21] Womersley J R 1955 *J. Physiol.* **127** 553
[22] Crandall I B 1926 *Theory of Vibrating Systems and Sound* (New York: D Van Nostrand Comp., Inc.)
[23] Sexl T 1930 *Z. Phys.* **61** 349
[24] Lambossy P 1952 *Helv. Phys. Acta* **25** 371
[25] Uchida S 1956 *Z. Angew. Math. Phys.* **7** 403
[26] Richardson E G 1928 *Proc. Phys. Soc. Lond.* **40** 206
[27] Sheen H J, Hsu C J, Wu T W, Chang C C, Chu H C, Yang C Y and Lei U 2008 *Microfluid. Nanofluid.* **4** 331
[28] Gilbertson R G and Busch J D 1996 *J. Br. Interplanet. Soc.* **49** 129
[29] Laser D J and Santiago J G 2004 *J. Micromech. Microeng.* **14** R35
[30] Bretherton F 1961 *J. Fluid Mech.* **10** 166
[31] Park C-W and Homsy G M 1984 *J. Fluid Mech.* **139** 291
[32] Schwartz L W, Princen H M and Kiss A D 1986 *J. Fluid Mech.* **172** 259
[33] Ratulowski J and Chang H-C 1989 *Phys. Fluids* A **1** 1642
[34] Chio H, Jensen M J, Wang X, Bruus H and Attinger D 2006 *J. Micromech. Microeng.* **16** 143
[35] Brennen C E 1995 *Cavitation and Bubble Dynamics* (New York: Oxford University Press)
[36] Fuerstman M J, Lai A, Thurlow M E, Shevkoplyas S S, Stone H A and Whitesides G M 2007 *Lab Chip* **7** 1479
[37] Landau L D and Lifshitz E M 1986 *Theory of Elasticity (A Course of Theoretical Physics vol 7)* 3rd edn (Oxford: Pergamon)
[38] Sundström B (ed) 1999 *Handbok och formelsamling i Hållfasthetslära* 2nd edn (Stockholm: Institutionen för hållfasthetslära, KTH)
[39] Osswald T A, Baur E, Brinkmann S, Oberbach K and Schmachtenberg E 2006 *International Plastics Handbook* (Munich: Carl Hanser)
[40] Womersley J R 1957 *Tech. Rep.* Wright Air Development Center 56-614
[41] Morgan G W and Kiely J P 1954 *J. Acoust. Soc. Am.* **26** 323
[42] Morgan G W and Ferrante W R 1955 *J. Acoust. Soc. Am.* **27** 715
[43] Moens A I 1878 *Die Pulskurve* (Leiden: Brill)
[44] Korteweg D J 1878 *Ann. Phys. Chem. (NS)* **5** 52